J Nanopart Res (2020) 22: 44
https://doi.org/10.1007/s11051-020-4763-3

RESEARCH PAPER

Structural and frequency-dependent dielectric properties of $(SnO_2)_{1-x}(Fe_2O_3)_x$

S.A. Saleh · I.A. Abdel-Latif · A.M. Abdel Hakeem · E.M.M. Ibrahim

Received: 1 November 2019 / Accepted: 24 January 2020 / Published online: 6 February 2020

Abstract A series of iron-substituted tin dioxide ceramics with composition $Sn_{x-1}Fe_xO_2$ was synthesized using a conventional solid-state method in order to investigate its detailed structural and dielectric properties. Samples formed in the tetragonal structure with grain sizes of around 88–48 nm. Reduction in grain size was found because of the suppression in the grain growth with Fe addition. From FTIR analysis, a broad peak was centered on 650 cm^{-1} due to Sn–O vibration. Many Raman-active phonon modes observed for as prepared samples. The Fe substitution in SnO_2 essentially changes the position of modes, where all the modes shifted to a lower wave number. For all the samples, frequency-dependent dielectric and AC conductivity measurements collected at room temperature and in the frequency range from 75 kHz to 10 MHz. In this frequency range, large dielectric dispersion was noted. According to our analysis of electrical properties of the samples under study, it is found that the conduction mechanism in these materials is based only on a small polaron.

Keywords Fe–tin dioxide · Raman spectroscopy · Dielectric constant · AC conductivity · Nanostructures

This article is part of the topical collection on *Nanotechnology in Arab Countries*, Guest Editor: Sherif El-Eskandarany

Electronic supplementary material The online version of this article (https://doi.org/10.1007/s11051-020-4763-3) contains supplementary material, which is available to authorized users.

S. Saleh · A. A. Hakeem · E. Ibrahim
Physics Department, Faculty of Science, Sohag University, Sohag 82524, Egypt

S. Saleh (✉) · I. Abdel-Latif
Physics Department, College of Science & Arts, Najran University, P.O. Box 1988, Najran, Kingdom of Saudi Arabia
e-mail: ihab_abdellatif@yahoo.co.uk

I. Abdel-Latif
Advanced Materials and Nano-Research Centre, Najran University, P.O. Box 1988, Najran 11001, Saudi Arabia

I. Abdel-Latif
Reactor Physics Department, NRC, Atomic Energy Authority, Abou Zabaal, P.O. 13759, Cairo, Egypt

Introduction

Electroceramics can be treated as a model because of their rich physical properties and relatively simple structure. They have wide applications in capacitors and memory devices. For capacitive and memory devices, ceramics should have colossal dielectric constant (CDC) (Thakur et al. 2013, Dhahri et al. 2011). From the practical point of view, tin dioxide exhibits rich and interesting physical properties because of the relationships between its electrical properties and several parameters (porosity, grain boundary barriers, crystallite size, temperature, etc.) (Abdel-Latif and Saleh 2012). Additionally, SnO_2 is chemically, mechanically, and thermally stable. Its stable rutile phase and the natural non-stoichiometry are key parameters to use these materials (Raju et al. 2018, Azam et al., 2010a, Saleh et al., 2016a, Bargougui et al. 2014, Korotcenkov and Cho 2009, Kocemba and Rynkowski 2011). Moreover, it is

easy to prepare them in the ceramic form thus enable us to use them efficiently.

Looking at the large number of publications, a few of them were devoted to the dielectric properties. We can get valuable information deal with the localized electric charge carrier behavior and enable us to understand the mechanism of dielectric polarization. Furthermore, the study on structure and dielectric properties of these materials will help to get overall knowledge about the essence of the loss existing in such compounds in addition to conduction mechanism (Khor et al. 2009).

It is widely proved that one of the essential prerequisites for justifying and comparing the results on this kind of compositions is full characterization of the synthesized materials. The morphology, the grain size distribution, and the chemical composition are the key factor which play very important role in the physicochemical properties of these materials. SnO_2 is a semiconductor so it is considered as a model system in the present study because of its excellent properties.

From the semiconductor technologies point of view, the control of various properties of the selected material may be achieved as a result of the incorporation of impurities or defects into the lattice. So, the doping process in SnO_2 compound became interesting point for research that enable to improve its electrical and microstructural properties (Drake and Seal, 2007, Lahouli et al. 2019, Xu et al. 2005, Drake et al. 2007). Low valency cations, such as trivalent iron, are particularly interesting elements for substitution. Iron is a particularly interesting dopant for substitution in tin dioxide, where an increase in the Debye length was obtained as a result of carrier concentration decrease and hence electrical resistance increased (Galatsis et al. 2003).

In capacitors, SnO_2 was implemented in the nano-scale ceramic form where there is a large ratio between the surface and the volume nano-range. The big difference in its electrical properties was noted depending on the crystallinity of this material (*Nalwa* 2000). This behavior may be attributed to the following parameters: the modification in band structure, the quantum confinement of carriers, and the contribution of the grain boundaries in the nano-scale.

From the applications point of view, a high dielectric constant and a low dielectric loss are generally required together with AC conductivity. Moreover, the influence of both of the frequency and the composition on the dielectric parameters offers much more understanding to the dielectric behavior, which may help to find a good interpretation of the conduction mechanisms.

The effect of iron doping on the structural and electrical properties of polycrystalline tin dioxide ceramics of the nano-scale was studied in this work. The dielectric parameter data were given in terms of frequency dependent. Moreover, structure and microstructure were studied in details and their correlation with electric properties for the pure and doped SnO_2 ceramics.

Experimental details

The ceramic samples of chemical formula $Sn_{1-x}Fe_xO_2$ ($x = 0.00, 0.02, 0.04, 0.06, 0.08, 0.10, 0.12, 0.16, 0.18$) were prepared by means of a conventional solid-state technique from the mixture of stoichiometric amounts of high purity oxides (SnO_2 and Fe_2O_3). Starting materials are Sigma–Aldrich oxides. The solid-state reaction method is more suitable for producing oxide materials rather than other methods (Dodiya 2013). The mixture was pressed under 5 ton cm^{-2} and annealed at temperature 1423 K in air for 24 h. The cooling process was done in the natural furnace temperature. This annealing followed by gradual cooling enables iron ions to get through tin dioxide and occupy some positions of Sn as shown in Scheme 1.

The prepared samples were characterized by various techniques. The step-scan X-ray diffraction (XRD) measurements were carried out at room temperature using a PANalytical X'Pert PRO diffractometer with Cu (K_α) radiation ($\lambda = 1.5406$ Å), with step of 0.02°. The counting time of each step was 1 s and starting angle was 10° up to 90°. A field emission scanning electron microscope (FESEM, JEOL JSM-7600F) was used to study the morphology of the samples and their chemical purity was checked by energy-dispersive spectroscopy (EDS). Raman spectra were performed using an Ar laser PerkinElmer spectrometer, in the wavelength of 514.5 nm. The infrared spectra were collected using a FTIR PerkinElmer spectrometer to check the bonding between different atoms as well as the chemical information about the particles. Frequency-dependent dielectric parameters were measured using (LCR) meter (HP4284A) in the frequency range of 75 kHz–10 MHz at room temperature.

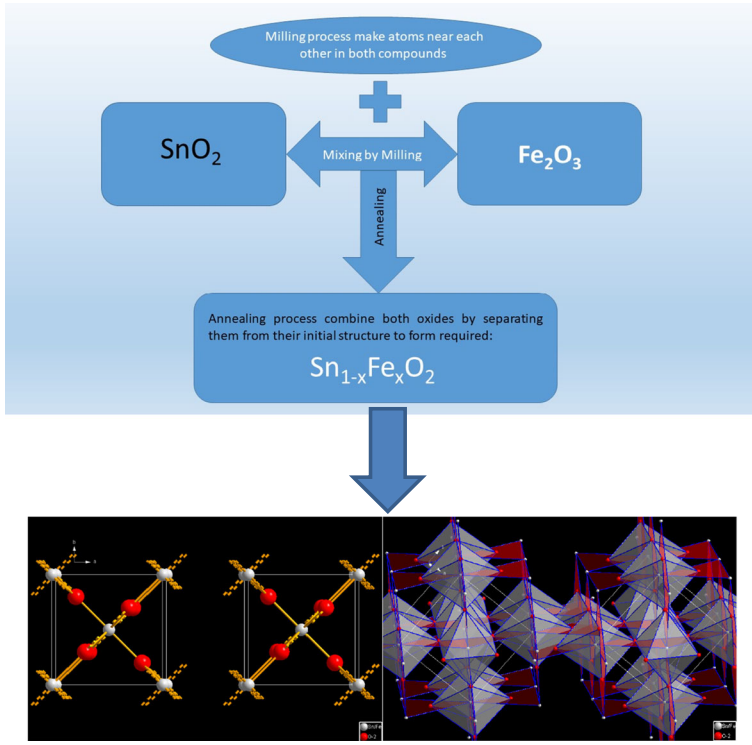

Scheme 1 The mechanism of forming $Sn_{1-x}Fe_xO_2$ using solid-state reaction

Results and discussion

X-ray diffraction analysis

XRD patterns of the synthesized Fe-doped SnO_2 ceramics with different doping concentrations are shown in Fig. 1 a. All XRD patterns were analyzed using FullProf software (Rodriguez-Carvajal 1993). It is clear that pure SnO_2 is formed in a single phase of the tetragonal crystal system with *P42/mnm* (136) space group where all the peaks in XRD pattern matches with the well-known crystal data identical to the JCPDS file no. 00-041-1445 (Jia et al. 2018). Because of Fe_2O_3 doping with so small concentrations $x = 0.02$, 0.04, and 0.06, we found that ten atoms were partially replaced with iron atoms and the crystal structure still in single phase (see Fig. 1b). When the concentration of Fe_2O_3 increased for the concentrations, which more than $x = 0.06$ another phase of Fe_2O_3 appeared in our samples (see Fig. 1c). All lattice parameters are given in Table 1. The resulted crystalline size δ after forming the required structure is calculated from the broadening of the XRD pattern where the broadening of Si as a standard sample is taken into consideration in order to avoid instrumental errors. The well-known Scherrer formula can give us this crystalline size δ as follows (Abdel-Latif 2011):

$$\delta = k\lambda/(B\sin\theta)$$

where B is full width at half maximum (FWHM), which may be represented as $B_{obs.}$–$B_{std.}$ ($B_{obs.}$ is given as FWHM of the observed sample; on the other hand, B_{std} is the standard sample FWHM). The crystalline size of pure SnO_2 is 180 nm which slightly decreased with Fe doping where it is 161 nm for $x = 0.02$. Then there is dramatic decrease with increasing Fe doping where it is 92 nm for $x = 0.06$.

Sn atoms in rutile structure occupy (0, 0, 0) position while oxygen atoms occupy at (0.3, 0.3, 0). Oxygen atoms (anions) are forming octahedra (Zhao et al. 2014) as shown in Scheme 1 where they surround tin atoms. Because of doping with Fe_2O_3 with different concentrations, we noted that the single phase of rutile structure is kept in $x = 0.02$, 0.04, and 0.06 as a result of the partial replacement of tin atoms by iron atoms. At concentration of $x > 0.06$, another phase was observed as Fe_2O_3 of hexagonal structure of space group R_{3c}. Lattice parameters are listed in Table 1.

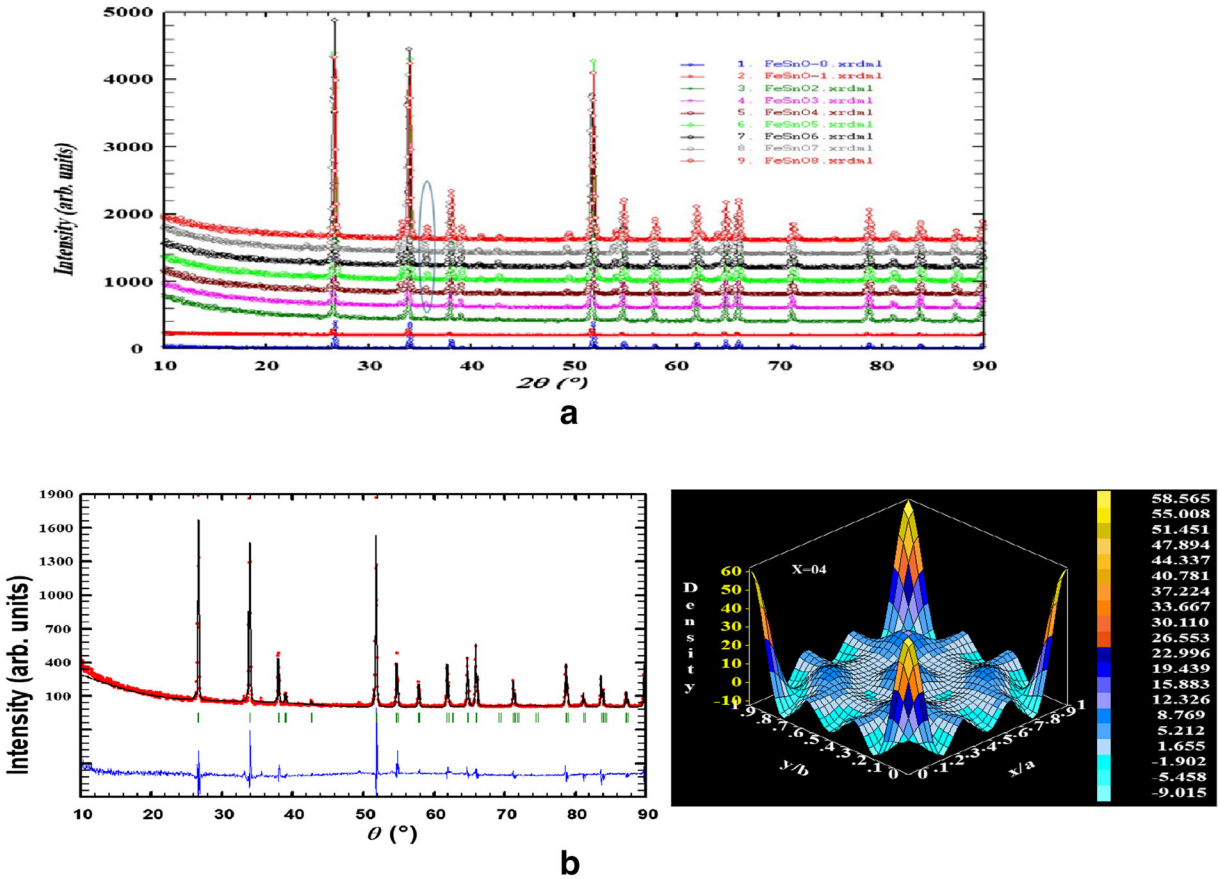

Fig. 1 **a** XRD patterns of all samples in and **b** XRD patterns of single phase in $x = 0.04$ refined by the Rietveld method and density of electrons map in unit cell

The calculations of the density of electrons $\rho(r)$, which are scattered from the unit cell of a crystal, are carried out based on Fourier as a subprogram in FullProf, regardless of the symmetry. A fast Fourier transform (FFT) is used for the calculation based on the following expression (Abdel-Latif, 2016):

Table 1 Structural parameters and porosity of SnO_2 doped with $x = Fe_2O_3$

x	SnO_2 ($P_{42/mnm}$)			Fe_2O_3 (R_{3c})		Porosity
	$a = b$ (Å)	c (Å)	c/a	$a = b$ (Å)	c (Å)	
0.0	4.7316	3.1778	0.6744			63.036
0.02	4.7415	3.1864	0.6688			21.282
0.04	4.7372	3.1864	0.6719			23.215
0.06	4.7349	3.1850	0.6719			31.567
0.08	4.7305	3.1838	0.6722	5.0332	13.7579	28.465
0.10	4.7215	3.1764	0.6733	5.0344	13.7670	39.158
0.12	4.7299	3.1827	0.6723	5.0293	13.7651	25.263
0.16	4.7457	3.1916	0.6711	5.0447	13.8045	32.423
0.18	4.7179	3.1761	0.6734	5.0185	13.7040	28.617
	Tetragonal			Hexagonal		

$$\rho(r) = \frac{1}{v}\sum_{\boldsymbol{H}} F(\boldsymbol{H})\exp\{-2\pi i(\boldsymbol{H}\cdot\boldsymbol{r})\}$$

It is clear from this equation $\rho(r)$ is a function of the following parameters: the unit cell volume (Vi), the reciprocal lattice vector (H), the vector position inside the unit cell (r), and the complex Fourier coefficients $F(H)$ (Abdel-Latif et al. 2019). The density of electrons inside the unit cell is calculated as shown in Fig. 1b for $Sn_{0.96}Fe_{0.04}O_2$ and all samples are shown in Suppl.1. One can note from the electron density maps that the density of electrons of both pure SnO_2 and $Sn_{0.98}Fe_{0.02}O_2$ is close to each other and is different from that of the other samples. Moreover, the electronic densities are comparably high in the first two samples and are lower for the concentrations $x \geq 0.04$. The higher concentrations samples have almost the same configuration of electronic density as shown in Suppl.1.

Microstructure analysis

Since the material properties depend strongly on its microstructure, all images of the prepared samples were done at room temperature by field emission scanning electron microscopy (FESEM). These images of $Sn_{1-x}Fe_xO_2$ ($x = 0.0$–0.18) samples are shown in Fig. 2 a–k. The FESEM micrographs revealed that the microstructure consists of very small, randomly oriented, homogenous, well-interlinked, and non-uniform (in shape and size) grains. Also, the micrographs show the agglomeration of nanoparticles. With incorporation of Fe^{3+} ions in SnO_2, the average grain size was reduced as shown in Table 1.

Further, energy-dispersive spectroscopy (EDS) spectra were done to check the purity of the chemical formula of the designed composites and they are illustrated in Suppl. 2 (a - k). The presence of only those elements, which comprise the prepared ceramics, is clear in the EDS patterns. On the other hand, it is a good indication to the formation of the required tin/iron oxide according to the proposed calculations.

Vibrational analysis

From Raman scattering, one can get valuable information about the crystallinity and size effects in our samples besides the resulting defect and vacancies (Kumar et al. 2017). The vibrational mode in the system could be described clearly based on the variations in position, intensity, and width of the Raman modes.

The six atoms existed in the SnO_2 unit cell give rise to 18 vibrational modes; four of them are Raman active (three non-degenerate modes, A_{1g}, B_{1g}, B_{2g}, and the doubly degenerate E_g) (Saleh et al., 2016b). According to these Raman-active modes, O atoms that vibrate on the other side Sn atoms are at rest. In the same direction, the double degenerate E_g mode vibrates while three non-degenerate modes (A_{1g}, B_{1g}, and B_{2g}) vibrate in the plane which is perpendicular to the c-axis respectively. Non-degenerate B_{1g} mode that include the rotation of all six oxygen atoms forming the octahedral site gives rise to the vibration around the c-axis (Matthias and Ulrike 2005).

Figure 3 a shows the room temperature Raman scattering spectra of parent (pure) and doped SnO_2 samples. The Raman modes are present at 777, 634, and 477 cm^{-1} corresponding to the three fundamental vibrational modes B_{2g}, A_{1g}, and E_g, respectively, describing the formation of the rutile crystal structure in these samples (Bhattacharjee and Ahmaruzzaman, 2015). Some extra peaks are observed at 225.27, 292.57, 408.79, and 607.68 cm^{-1} with increase in Fe concentration, which may be attributed to the nano-effect.

The atomic displacements may be found by Raman spectroscopy. The shift in the 634 and 477 cm^{-1} modes may be a result of the substitution of Sn^{4+} ions by small ions Fe^{3+}. The higher frequency mode (777 cm^{-1}) has almost disappeared. The observed broadening and the reduced intensities occurred in the peak imply the structural disorder with incorporation of Fe. The increase in the structural disorder appeared usually at nano-size (Gouadec and Colomban, 2007). Moreover, a decrease in the inversion centers density may allow to the appearance of the IR-active modes.

FTIR spectra of the wavenumber ranging 400–4000 cm^{-1} are shown in Fig. 3 b. That may help to describe the formation of fundamental absorption bands in the SnO_2- and Fe-doped SnO_2 systems. The nano-size effect of the Sn–O stretching vibrations is found in the region 400–800 cm^{-1}. In our case, the 647 cm^{-1} peak is assigned to Sn–O–Sn stretching mode formed by the condensation of adjacent hydroxyl groups (Reddy et al. 2016). The 545 cm^{-1} band is referred to terminal Sn–O vibration of the Sn–OH group. The bending vibration of adsorbed water molecules is observed at 1628 cm^{-1} (Ben Haj Othmen et al. 2018). A broad band, which is found at 3429 cm^{-1}, refers to O–H stretching vibration because of trapping of water molecules at the sample

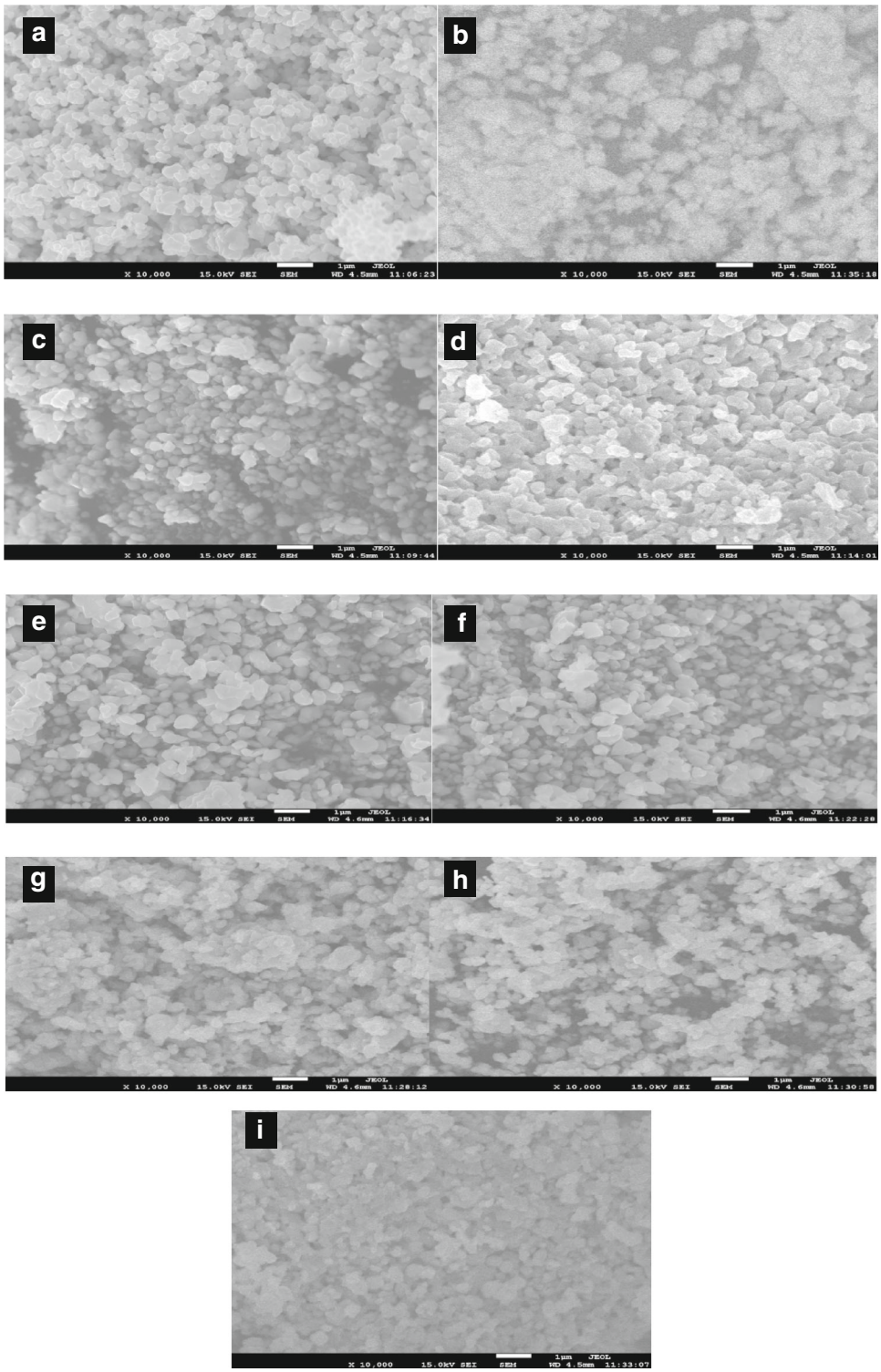

Fig. 2 **a**–**k** FESEM images of $Sn_{1-x}Fe_xO_2$ ceramics with $x = 0.00$–0.18

surface (Parthibavarman et al. 2014). Shift of the peaks towards the lower wavenumber that occurred in our case may be attributed to the defects in our samples as a result of increase of iron concentration.

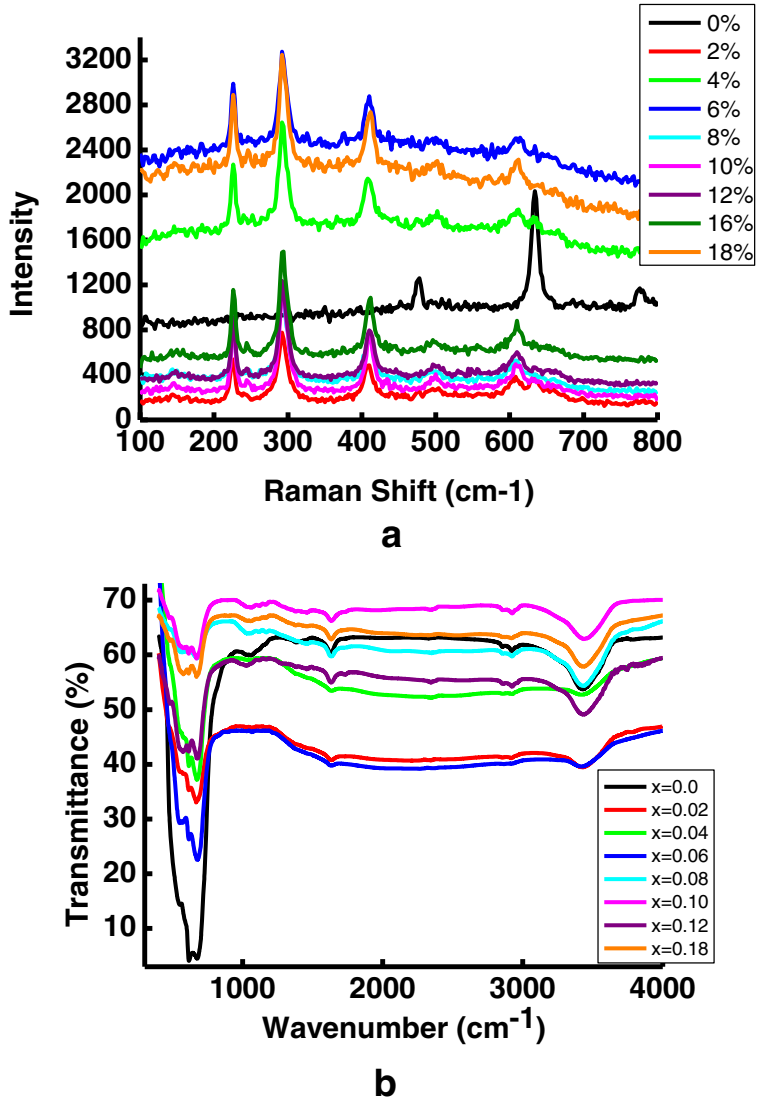

Fig. 3 **a** Raman spectra of all samples at room temperature. **b** FTIR of $Sn_{1-x}Fe_xO_2$ ($x = 0.00$–0.18) ceramics

Dielectric analysis

For engineering applications in electronic materials, the dielectric properties of usual interest are the complex dielectric constant ε^*. This quantity described as (Naseem et al. 2018) $\varepsilon* = \varepsilon' + j\varepsilon''$, ε' called dielectric constant, is the real part of permittivity, which describes the material capacity to store charge and the imaginary part of permittivity is namely dielectric loss ε'' that describes the energy needed for molecular motion or the loss in energy because of the polarization and ionic conduction (Khor et al. 2009).

The permittivity of a material is an indication not only to the molecular relaxation but also to the transport processes. It may depend on many parameters such as the material structure, composition, and synthesis method. To understand role of the following parameters, microstructure, intergranular potential barrier, and composition on the electrical properties of any material, the value of (ε') can be obtained using relation:

$$\varepsilon' = Cd/\varepsilon_o A$$

where A is the sample area, ε_o free space permittivity, C is the effective capacitance, and d is the sample thickness. The imaginary part of the permittivity (ε'') which is calculated using the formula: $\varepsilon'' = \varepsilon' \tan\delta$, where $\tan\delta = \tan(90 - \phi)$ is the dielectric loss factor and it is

related to the energy loss from the applied field into the sample to be termed as dielectric loss.

The dependence of dielectric constant (ε') and dielectric loss factors (ε'') of undoped and Fe-doped SnO_2 ceramics at room temperature and in the frequency range from 75 kHz to 10 MHz is illustrated in Fig. 4. It is quite clear that all samples are describing the normal dielectric behavior for both ε' and ε'' where the decrease occurred with an increase in frequency. This occurred in the low-frequency region because of the inability of the electric dipoles to be in pace with the frequency of applied electric field at high frequency (Kundys et al. 2008). The obtained high values for both two factors at lower frequencies region are described according to the space charge polarization resulted from the inhomogeneities present in the dielectric structure, viz. porosity in the system. The change in the dielectric may depend on the nature of material (Kumar et al. 2016). Moreover, all the samples exhibit large dielectric dispersion in the under investigation frequency range. That may explain the high value of dielectric constant at low frequency and the low value of dielectric constant as a result of the high value of the frequency. Among all the samples, the lowest dielectric dispersion achieved for $Sn_{0.9}Fe_{0.1}O_2$ exhibits while the $Sn_{0.98}Fe_{0.02}O_2$ gives highest dielectric dispersion. The decrement in both ε' and ε'' is attributed to the dielectric relaxation.

Dielectric loss of pure and iron-doped SnO_2 samples displayed the same behavior of the dielectric constant-frequency dependent as shown in Fig. 4 c. It is also noted that as a result of adding Fe, low tangent was loss compared with the undoped SnO_2 sample. Two main factors affected the dielectric loss: resistive loss and relaxation loss. Energy is utilized by the mobile charges in resistive loss case, while in the case of relaxation loss, the dipoles relaxation give rise to the dissipation of energy (Sharma et al. 2014). High dielectric losses obtained at lower frequency may attributed to the space charge polarization according to the Shockley–Read mechanism (Abdel-Latif et al. 2018), where at low and intermediate frequency, surface electrons may be captured by the impurities and defects in crystal lattice, and hence, the space charge polarization occurs (Abdel-Latif et al. 2018). Low dielectric loss observed at higher frequencies, in our case, may be attributed to the formation of defects dipoles originated because of the mix of valence states (Fe^{3+}/Fe^{2+} and Sn^{4+}/Sn^{2+}) (Mehraj et al. 2015). Looking at the high resistance of the grain boundary that is found in $T_{0.6}Co_{0.4}Fe_2O_4$, space charge polarization was produced as a result of the electronic accumulation at the grain boundary (Hcini et al. 2017).

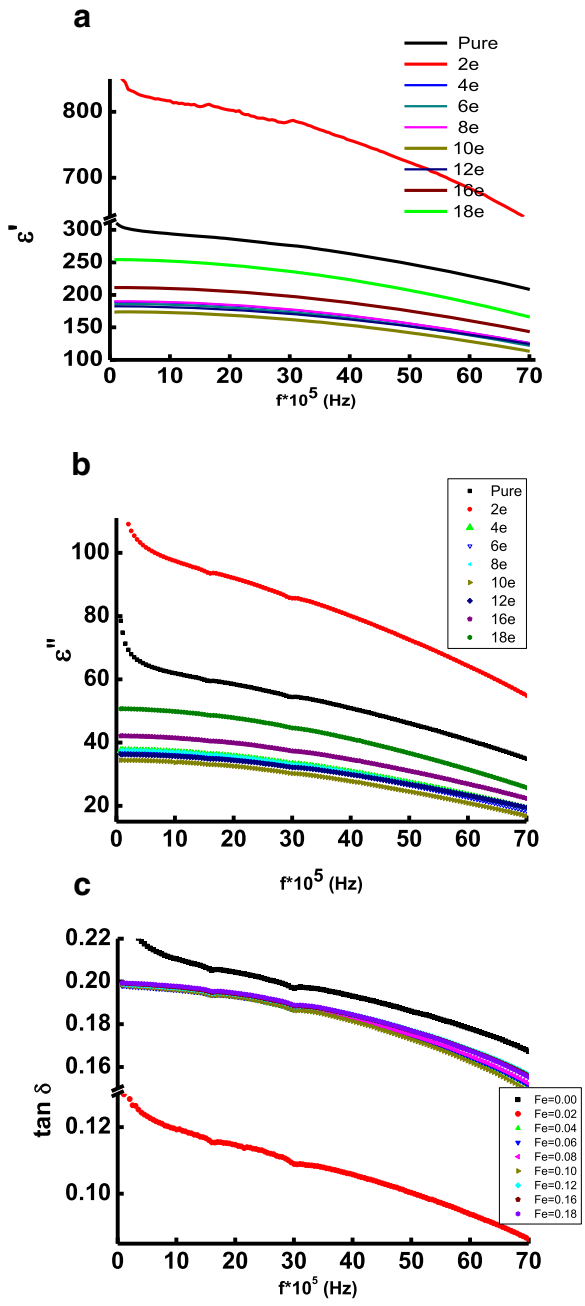

Fig. 4 **a** Variation of permittivity real part with frequency for all samples at 300 K. **b** Room temperature frequency dependence of imaginary part for all samples. **c** Tangent loss of all samples as function of frequency at room temperature

Both of the dielectric constant and dielectric loss at lower frequencies show a larger dispersion whereas they reach a low value at higher frequencies. On the basis of space charge polarization (Maxwell–Wagner bilayer) model, this behavior can be well explained and it is in good agreement with Koop's phenomenological theory (Godara et al. 2015). According to it, the origin of the space charge polarization may be explained because of the inhomogeneous dielectric materials that consist of large good-conducting grains surrounded by the low-conducting grain boundaries. The migration of charge carriers that occurred at low frequencies in interfacial, space charge, and polarization is predominate (Ahmad et al. 2018). Moreover, the relation between the space charges and the applied electric field at low frequency is the reason for the high dielectric constant value. On the other side, at higher frequency, no enough time to follow the applied electric field gives rise to the appearance of relaxation. The well-known polarization types that affect the total polarization are listed as follows: electronic, dipolar, ionic, and interfacial polarization. Dipolar and interfacial polarizations are taking charge of dielectric constant at lower frequency, while both of the electronic and the ionic polarizations are taking charge of dielectric constant at higher frequency. Electrons shift from the equilibrium position under the influence of electric field application, and hence cause polarization (Chandel et al., 2018).

To understand the conduction mechanism in present ceramics the AC conductivity (σ_{ac}) calculated with data available from the dielectric measurement by the empirical formula (Zhao et al. 2018):

$$\sigma_{ac} = 2\pi f \varepsilon_o \varepsilon' \tan\delta$$

where, f is the applied field frequency. The room temperature frequency dependence of AC conductivity for Fe-doped SnO_2 ceramics is shown in Fig. 5. The increase in AC conductivity as a result of the frequency of applied field is because this increase in frequency reinforces the electron hopping frequency (Azam et al., 2010b). From the charge carriers transfer point of view, charge carrier may transfer between localized states and the driving force generated through applied field associates the liberation of the trapped charges (Farea et al. 2008). The exchange interactions between the different metal ions have the main contribution to the conduction mechanism.

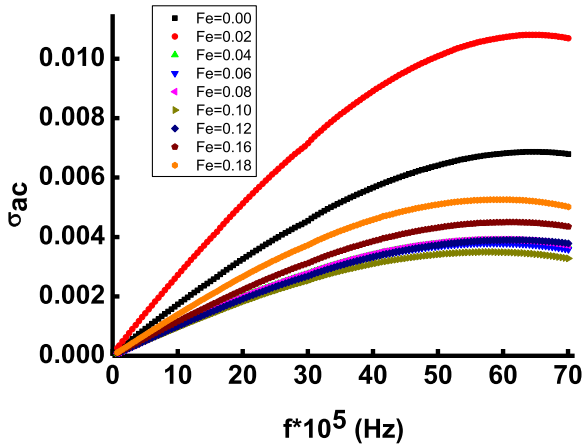

Fig. 5 AC conductivity versus frequency at room temperature for all samples

The frequency response of AC conductivity (σ_{ac}) in the investigated material can be interpreted according to the hopping or polaron mechanisms depending on the available free charge carriers. The motion of electros under the effect of electric field polarizes or distorts the lattice forming polarons. Small polaron are generated as a result of the spatial extension of such deformation or distortion over the lattice is of the order of the lattice constant while the generation of large polarons occurs when the deformation extends beyond the lattice constant. The AC conductivity decrease as a result of the increase of frequency that may give rise to large polaron

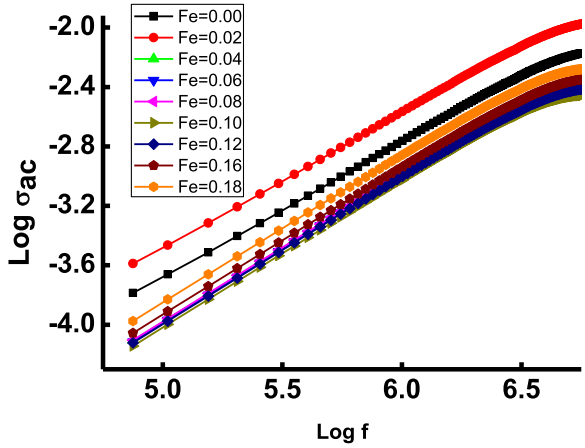

Fig. 6 Variation of log σ_{ac} with respect to log f for Fe-doped SnO_2 ceramics

model, whereas the opposite behavior explains small polaron model (Dhanalakshmi et al., 2016a, Dhanalakshmi et al., 2016b). Hence, the observed variation in (σ_{ac}) as a function of frequency in the present study is in accordance with small polaron mechanisms only. The involved electrons in hopping are responsible for electronic polarization in these compositions (Parthibavarman et al. 2014). The frequency-dependent AC conductivity of dielectric materials could be expressed by power law given by (Abo El Ata et al. 2006):

$$\sigma_{ac} = B\omega^n$$

where B and n are temperature and material intrinsic property dependent; B has the units of conductivity while n is dimensionless (Mehedi Hassan et al. 2012). The n value is deduced from the slope of the log σ_{ac} versus log f given in Fig. 6, and the linear fitting is an indication to the conduction as frequency dependent when n is less than one and greater than 0 ($0 < n < 1$) or frequency independent when $n = 0$ (Mehedi Hassan et al. 2012). The values of n less than one and greater than 0 ($n = 0.827$, 0.831, 0.835, 0.833, 0.836, 0.83, 0.848, 0.846, and 0.842) for all samples. According to the n values, in our samples, the conduction is frequency dependent and it is evident of the presence of small polarons only.

Conclusions

Because of Fe_2O_3 doping within a small concentrations ($x = 0.02$, 0.04, and 0.06), $Sn_{1-x}Fe_xO_2$ was found to have single phase and Sn atoms partially replaced by Fe atoms to hold the same symmetry of tetragonal crystal system of *P42/mnm* (136) space group.

There is a decrease in the dielectric constant and dielectric loss depending on the increase in frequency. Moreover, the dielectric parameters in the investigated samples are explained according to space charge polarization and to the Maxwell and Wagner's two-layer model. From the AC conductivity frequency-dependent measurements, a small polaron mechanism is pronounced. In the high-frequency region, the dielectric loss of high iron concentration is near zero implying that the material is promising for high-frequency device use.

Funding information One of the authors (Dr. Ihab) is thankful to the Deanship of Scientific Research in Najran University for their financial support NU/ESCI/16/063 in the frame of the local scientific research program support.

Compliance with ethical standards

Conflict of interest The authors declare that they have no conflict of interest.

References

Abdel-Latif IA, Saleh SA (2012) Effect of iron doping on the physical properties of europium manganites. J Alloys Compd 530:116–120

Abdel-Latif IA (2011) Study on the effect of particle size of strontium - ytterbium manganites on some physical properties. AIP Conf Proc 1370:108–115. https://doi.org/10.1063/1.3638090

Abdel-Latif IA (2016) Study on structure, electrical and dielectric properties of $Eu_{0.65}Sr_{0.35}Fe_{0.3}Mn_{0.7}O_3$. IOP Conf Series: Mater Sci Eng 146:012003. https://doi.org/10.1088/1757-899X/146/1/

Abdel-Latif IA, al-Hajji LA, Faisal M, Ismail AA (2019) Doping strontium into neodymium manganites nanocomposites for enhanced visible light driven photocatalysis. Sci Rep 9: 13932. https://doi.org/10.1038/s41598-019-50393-9

Abdel-Latif IA et al (2018) Magnetocaloric effect, electric, and dielectric properties of $Nd_{0.6}Sr_{0.4}Mn_xCo_{1-x}O_3$ composites. *J Magn Magn Mater* 457:126–134. https://doi.org/10.1016/j.jmmm.2018.02.087

Abo El Ata AM, El Nimr MK, Attia SM, El Kony D, Al-Hammadi AH (2006) Studies of AC electrical conductivity and initial magnetic permeability of rare-earth-substituted Li–Co ferrites. J Magn Magn Mater 33:297. https://doi.org/10.1016/j.jmmm.2005.01.085

Ahmad N, Khan S, Ansari MMN (2018) Microstructural, optical and electrical transport properties of Cd-doped SnO_2 nanoparticles. Mater Res Express 5(3):035045

Azam A et al (2010a) Study of electrical properties of nickel doped SnO_2 ceramic nanoparticles. J Alloys Compd 506:237–242. https://doi.org/10.1016/j.jallcom.2010.06.184

Azam A, Ahmed AS, Chaman M, Naqvi AH (2010b) Investigation of electrical properties of Mn doped tin oxide nanoparticles using impedance spectroscopy. J Appl Phys 108:094329. https://doi.org/10.1063/1.3506691

Bargougui R, Oueslati A, Schmerber G, Ulhaq-Bouillet C, Colis S, Hlel F, Ammar S, Dinia A (2014) Structural, optical and electrical properties of Zn-doped SnO_2 nanoparticles synthesized by the co-precipitation technique. J Mater Sci Mater Electron 25:2066–2071. https://doi.org/10.1007/s10854-014-1841-2

Ben Haj Othmen W et al (2018) Effect of high Fe doping on Raman modes and optical properties of hydrothermally prepared SnO_2 nanoparticles. Mater Sci Semicond Process 77: 31–39. https://doi.org/10.1016/j.mssp.2017.12.014

Bhattacharjee A, Ahmaruzzaman M (2015) Facile synthesis of SnO_2 quantum dots and its photocatalytic activity in the

degradation of eosin Y dye: a green approach mater. Lett. 139:418. https://doi.org/10.1016/j.matlet.2014.10.121

Dhanalakshmi B et al (2016a) Impedance spectroscopy and dielectric properties of multiferroic $BiFeO_3/Bi_{0.95}Mn_{0.05}FeO_3$–$Ni_{0.5}Zn_{0.5}Fe_2O_4$ composites. Ceram Int 42:2186–2197. https://doi.org/10.1016/j.ceramint.2015.10.005

Dhanalakshmi B et al (2016b) Effects of Mn doping on structural, dielectric and multiferroic properties of $BiFeO_3$ nanoceramics. J Alloys Compd 676:193–201. https://doi.org/10.1016/j.jallcom.2016.03.208

Dhahri A, Rhouma FIH, Dhahri J, Dhahri E, Valente MA (2011) Structural and electrical characteristics of rare earth simple perovskite oxide $La_{0.57}Nd_{0.1}Pb_{0.33}Mn_{0.8}Ti_{0.2}O_3$. Solid State Commun 151:738. https://doi.org/10.1016/j.ssc.2011.01.015

Drake C, Seal S (2007) Band gap energy modifications observed in trivalent in substituted nanocrystalline SnO_2. Appl Phys Lett 90:233117. https://doi.org/10.1063/1.2746407

Drake C, Amalu A, Bernard J, Seal S (2007) Enhancing the low temperature hydrogen sensitivity of nanocrystalline SnO_2 as a function of trivalent dopants. J Appl Phys 101:104307. https://doi.org/10.1063/1.2732498

Dodiya N, Varshney D (2013) Structural properties and Raman spectroscopy of rhombohedral $La_{1-x}Na_xMnO_3$ ($0.075 \leq x \leq 0.15$). J Mol Struct 1031:104–109. https://doi.org/10.1016/j.molstruc.2012.07.037

Chandel S, Thakur P, Thakur SS, Kanwar V, Tomar M, Gupta V, Thakur A (2018) Effect of non-magnetic Al^{3+} doping on structural, optical, electrical, dielectric and magnetic properties of $BiFeO_3$ ceramics. Ceram Int 44:4711–4718. https://doi.org/10.1016/j.ceramint.2017.12.053

Farea AMM, Kumar S, Batoo KM, Yousef A, Lee CG, Alimuddin (2008) Structure and electrical properties of $Co_{0.5}Cd_xFe_{2.5-x}O_4$ ferrites. J Alloys Compd 464:361–369. https://doi.org/10.1016/j.jallcom.2007.09.126

Galatsis K et al (2003) P- and n-type Fe-doped SnO_2 gas sensors fabricated by the mechanochemical processing technique. Sensors Actuators B Chem 93(2003):562–565. https://doi.org/10.1016/S0925-4005(03)00233-8

Godara P et al (2015) Crystal structure refinement, dielectric and magnetic properties of Sm modified $BiFeO_3$ multiferroic. J Mol Struct 1097:207–213. https://doi.org/10.1016/j.molstruc.2015.05.022

Gouadec G, Colomban P (2007) Raman spectroscopy of nanomaterials: how spectra relate to disorder, particle size and mechanical properties. Prog Cryst Growth Charact Mater 53(1):1–56. https://doi.org/10.1016/j.pcrysgrow.2007.01.001

Nalwa HS (2000) Handbook of nanostructured materials and nanotechnology. Elsevier Inc, Academic, USA

Hcini S et al (2017) Structural, dielectric and complex impedance properties of $T_{0.6}Co_{0.4}Fe_2O_4$ (T=Ni, Mg) ferrite nanoparticles prepared by sol gel method. Ceram Int 43:2529–2536. https://doi.org/10.1016/j.ceramint.2016.11.055

Jia C et al (2018) Preparation of anatase/rutile TiO_2/SnO_2 hollow heterostructures for gas sensor. J Alloys Compd 769:521–531. https://doi.org/10.1016/j.jallcom.2018.08.035

Kocemba I, Rynkowski J (2011) The influence of catalytic activity on the response of Pt/SnO2 gas sensors to carbon monoxide and hydrogen. Sensors Actuators B Chem 155:659–666. https://doi.org/10.1016/j.snb.2011.01.026

Korotcenkov G, Cho BK (2009) Thin film SnO_2-based gas sensors: film thickness influence. Sensors Actuators B Chem 142:321–330. https://doi.org/10.1016/j.snb.2009.08.006

Khor SF, Talib ZA, Sidek HAA, Daud WM, Ng BH (2009) Effects of ZnO on dielectric properties and electrical conductivity of ternary zinc magnesium phosphate glasses. American J Appl Sci 6:1010–1014. https://doi.org/10.3844/ajassp.2009.1010.1014

Kumar V, Singh K, Kumar A, Kumar M, Singh K, Vij A, Thakur A (2017) Effect of solvent on crystallographic, morphological and optical properties of SnO_2 nanoparticles. Mater Res Bull 85:202–208. https://doi.org/10.1016/j.materresbull.2016.09.020

Kumar A, Sharma P, Yang W, Shen J, Varshney D, Li Q (2016) Effect of La and Ni substitution on structure, dielectric and ferroelectric properties of $BiFeO_3$ ceramics. Ceram Int 42:14805–14812. https://doi.org/10.1016/j.ceramint.2016.06.113

Kundys B, Maignan A, Martin C, Nguyen N, Simon C (2008) Magnetic field induced ferroelectric loop in $Bi_{0.75}Sr_{0.25}FeO_{3-\delta}$. Appl Phys Lett 92:112905. https://doi.org/10.1063/1.2890714

Lahouli R et al (2019) Investigation of annealing effects on the physical properties of $Ni_{0.6}Zn_{0.4}Fe_{1.5}Al_{0.5}O_4$ ferrite. RSC Adv 9:19949–19964. https://doi.org/10.1039/C9RA02238D

Matthias B, Ulrike D (2005) The surface and materials science of tin oxide. Prog Surf Sci 79:47–15. https://doi.org/10.1016/j.progsurf.2005.09.002

Mehedi Hassan M et al (2012) Structural and frequency dependent dielectric properties of Fe^{3+} doped ZnO nanoparticles. Mater Res Bull 47:3952–3958. https://doi.org/10.1016/j.materresbull.2012.08.015

Mehraj S et al (2015) Structural, electrical and magnetic properties of (Fe, Co) co-doped SnO_2 diluted magnetic semiconductor nanostructures. Phys E Low-dimensional Syst Nanostructures 65:84–92. https://doi.org/10.1016/j.physe.2014.08.016

Naseem S et al (2018) Dielectric response and room temperature ferromagnetism in Cr doped anatase TiO_2 nanoparticles. J Magn Magn Mater 447:155–166. https://doi.org/10.1016/j.jmmm.2017.09.051

Parthibavarman M, Vallalperuman K, Sathishkumar S, Durairaj M, Thavamani K (2014) A novel microwave synthesis of nanocrystalline SnO_2 and its structural optical and dielectric properties. J Mater Sci Mater Electron 25:730–735. https://doi.org/10.1007/s10854-013-1637-9

Raju MJS et al (2018) Structural and optical properties of Sb doped SnO_2 nanopowders synthesized by nebulized spray pyrolysis. Mater Today: Proceed 5:10097–10103. https://doi.org/10.1016/j.matpr.2017.11.005

Reddy CV et al (2016) Structural and optical properties of vanadium doped SnO_2 nanoparticles with high photocatalytic activities. J Lumin 179:26–34. https://doi.org/10.1016/j.jlumin.2016.06.036

Rodriguez-Carvajal (1993) Recent advances in magnetic structure determination by neutron powder diffraction. Physica B 192:55–69. https://doi.org/10.1016/0921-4526(93)90108-I

Saleh SA et al (2016a) Effect of Fe doping on the electrical and magnetic properties of $Sn_{1-x}Fe_xO_2$ nanoparticles Eur. Phys J Appl Phys 73:30401. https://doi.org/10.1051/epjap/2016150539

Saleh SA, Ibrahim AA, Mohamed SH (2016b) Structural and optical properties of nanostructured Fe-doped SnO_2. Acta Phys Polo A 129:1220–1225. https://doi.org/10.12693/APhysPolA.129.1220

Sharma HB, Nomita DK, Gupta V, Lee JH, Bobby SS (2014) Ac electrical conductivity and magnetic properties of $BiFeO_3$–$CoFe_2O_4$ nanocomposites. J Alloys Compd 599:32–39. https://doi.org/10.1016/j.jallcom.2014.02.024

Thakur S, Pandey OP, Singh K (2013) Structural and dielectric properties of $Bi_{1-x}Sr_xMnO_3$ ($0.40 \leq x \leq 0.55$). Ceram Int 39: 6165. https://doi.org/10.1016/j.ceramint.2013.01.035

Xu G, Zhang Y-W, Sun X, Xu C-L, Yan C-H (2005) Synthesis, structure, texture, and CO sensing behavior of nanocrystalline tin oxide doped with Scandia. J Phys Chem B 109:3269–3278. https://doi.org/10.1021/jp045282u

Zhao W et al (2014) Synthesis, characterization, and photocatalytic properties of SnO_2/rutile TiO_2/anatase TiO_2 heterojunctions modified by Pt. J Phys Chem C 118:23117–23125. https://doi.org/10.1021/jp506495a

Zhao N, Fana H, Ren X, Ma J, Bao J, Guo Y, Zhou Y (2018) Dielectric, conductivity and piezoelectric properties in (0.67-x)$BiFeO_3$-0.33$BaTiO_3$-x$SrZrO_3$ ceramics. Ceram Int 44: 18821–18827. https://doi.org/10.1016/j.ceramint.2018.07.116